Crystal Structure and Spectroscopic Analysis of the Compatible Solute Nγ-Acetyl-L-2,4-Diaminobutyric Acid

Lea Martin [1], **Wilhelm Klein** [2], **Sebastian P. Schwaminger** [1], **Thomas F. Fässler** [2] **and Sonja Berensmeier** [1,*]

[1] Bioseparation Engineering Group, Department of Mechanical Engineering, Technical University of Munich, 85748 Garching, Germany; l.martin@tum.de (L.M.); s.schwaminger@tum.de (S.P.S.)

[2] Department of Chemistry, Technical University of Munich, 85748 Garching, Germany; wilhelm.klein@tum.de (W.K.); thomas.faessler@lrz.tum.de (T.F.F.)

[*] Correspondence: s.berensmeier@tum.de; Tel.: +49-89-289-15750

Abstract: Compatible solutes are low molecular weight, highly water-soluble and neutrally net-charged molecules with various protective functionalities that accumulate and are produced in microorganisms. Their multi-purpose functionalities, also adaptable in vitro, make them potential components in healthcare and cosmetic products. One promising but insufficiently examined representative of this molecule class is Nγ-acetyl-L-2,4-diaminobutyric acid (γ-NADA), the metabolic precursor of ectoine. Here, we demonstrate the crystallization ability of γ-NADA by using cooling crystallization in aqueous solvents and find that it forms rod-shaped crystals. According to a single crystal structure determination, γ-NADA is orthorhombic with space group $P2_12_12_1$ and a = 5.3647(1), b = 8.3652(2), c = 16.9149(5) Å, Z = 4, R_1 = 3.48%, wR_2 = 7.33% (all data). Additionally, γ-NADA is analyzed via Raman, IR, ^1H, and ^{13}C NMR spectroscopy.

Keywords: compatible solute; amino acid; NADA; (2S)-4-acetamido-2-aminobutanoic acid; small molecule; crystallization; crystal structure; Raman; infrared spectroscopy

1. Introduction

Facing osmotic pressure in saline environments, halophilic bacteria produce and take up so-called compatible solutes to compensate for osmotic pressure and the effects of salt. Compatible solutes are of low molecular weight, and are polar and highly water-soluble molecules. In addition, they are uncharged at a neutral pH. Most importantly, they do not interfere with cell metabolism, i.e., they are compatible with the organism [1], creating an adaptive strategy to changes in the surrounding salinity. The preferential-exclusion model [2–4] describes the functionality of the compatible solutes in the solution, stabilizing the hydration layer [5,6] by keeping themselves away from the vicinity of proteins.

Compatible solutes consist of a broad diversity of molecules, ranging from sugars, polyols, amino acids and their acetylated derivatives [7–10], which are used by bacteria, archaea, and eukarya [11] to perform a large spectrum of protective functions [10,12–14]. Thus potential application areas of compatible solutes range from skincare [15,16] and treatment against respiratory infections [17,18] to cancer treatments [19,20] and process optimization [21–24]. Additionally, the formulation of biologicals and proteins has also been investigated [25–28].

Ectoine is one of the most successful compatible solutes and is biotechnologically produced in tons per year [29] for use in various cosmetic products. It is produced by the moderate halophilic γ-proteobacterium *Halomonas elongata* and enables the organism to grow in high salinity solutions of

more than 30% NaCl [30]. Figure 1 shows the metabolic synthesis of ectoine in *H. elongata*, which begins with L-aspartate. Here, the precursor molecule of ectoine, Nγ-acetyl-L-2,4-diaminobutyric acid (IUPAC nomenclature: (2S)-4-acetamido-2-aminobutanoic acid) (γ-NADA), a linear amino acid derivative, is converted to ectoine in a cyclic condensation reaction with the help of ectoine synthase (EctC) [31].
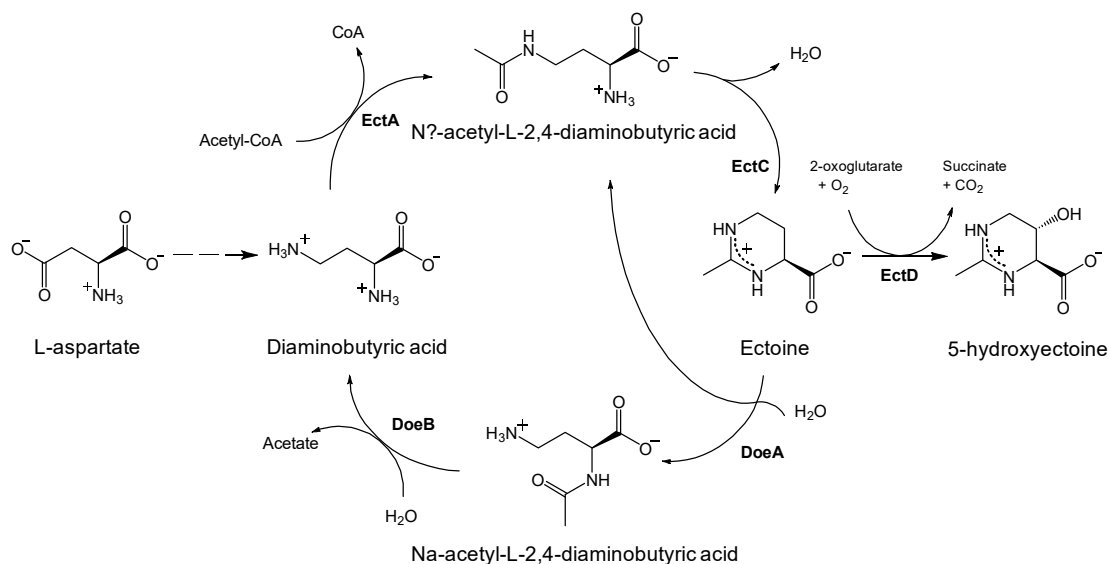
Figure 1. Ectoine synthesis pathway in *H. elongata*, starting with L-aspartate. Nγ-acetyl-L-2,4-diaminobutyric acid (γ-NADA) is enzymatically converted from diaminobutyric acid with the help of L-2,4-diaminobutyric acid transaminase (EctA). Ectoine synthase (EctC) catalyzes the ring formation to ectoine and ectoine hydroxylase (EctD), the hydroxylation to 5-hydroxyectoine. Ectoine hydrolase (DoeA) hydrolyses ectoine to Nα-acetyl-L-2,4-diaminobutyric acid, and Nα-acetyl-L-2,4-diaminobutyric acid deacetylase (DoeB) finally closes the cycle to diaminobutyric acid. Adapted with permission from [32].

γ-NADA was first discovered by Liss (1962) in latex produced by *Euphorbia pulcherrima* [33]. However, its interesting, osmoprotective functionality was not discovered until 1997, when Cánovas et al., (1997) created a *Halomonas elongata* mutant to further study γ-NADA [34]. This protective characteristic can also be gained by non-producing bacteria through γ-NADA uptake [35]. Cánovas et al., (1999) also demonstrated the functional integrity of a thermally treated enzyme in the presence of γ-NADA in vitro, which was even better than in the presence of the established ectoine [36]. This finding indicates the protective application of γ-NADA beyond natural osmoprotection. However, the molecule itself and its ability to be utilized as an alternative in the compatible solute market has been investigated rarely.

Thus, we conduct a deeper characterization of γ-NADA by showing its crystallization ability. The crystallization of biomolecules is a crucial step to analyze the structure, using X-ray diffraction, and therefore their physical properties. The structure, shape and size of the obtained crystal allow possible conclusions to be drawn about the physical behavior of the solid—e.g., stability and bioavailability. Further, they define the separation and purification ability of the biological molecule and form the bases of downstream processes. Here, these processes benefit from a fast volume reduction, which is also possible in the early stages, and the required formulation and purification of the final product [37].

2. Materials and Methods

Hydrolyzed ectoine material (provide by bitop AG), containing Nγ-acetyl-L-2,4-diaminobutyric acid (γ-NADA), Nα-acetyl-L-2,4-diaminobutyric acid (α-NADA), ectoine, and sodium chloride (NaCl) was dissolved to maximum solubility overnight at 50 °C in H_2O. Saturated suspension was sterile filtered to avoid nucleation on foreign and undissolved particles. Further, γ-NADA was crystallized

with cooling down the saturated solution from 50 to 20 °C and incubated for at least 24 h under orbital shaking or stirring. γ-NADA crystals were identified with HPLC analysis, using a reversed-phase method with 65/35 ACN/H_2O, YMC-Pack Polyamine II 12 nm, S-5 μm, 250 × 4.6 mm ID column, 1 mL min^{-1} at 30 °C. Further, dried γ-NADA crystals were put on a microscope slide and visualized with the microscope Nikon Eclipse 50i, equipped with a CFI Plan Fluor 4-fold objective. Microscopic images were taken with a Nikon DS-2Mv digital camera.

Crystals of γ-NADA have been investigated by X-ray single-crystal diffraction. For data collection, the single crystals were fixed on the tip of a glass fiber and were positioned in a cold N_2 gas stream for the low-temperature measurements. Data collection was performed at 100 K, 200 K, and at 300 K, respectively, with a StadiVari (Mo Kα radiation) diffractometer (Stoe & Cie, Darmstadt, Germany) equipped with a PILATUS 300K detector (Dectris Ltd., Baden-Daettwil, Switzerland) and a Cryostream 800 system (Oxford Cryosystems, Oxford, United Kingdom). The structure was solved by Direct Methods (SHELXS-2014) [38] and refined by full-matrix least-squares calculations against F^2 (SHELXL-2014) [39]. All non-hydrogen atoms were treated with anisotropic displacement parameters. All hydrogen atoms have been located from the difference Fourier map and refined with free atomic coordinates and isotropic displacement parameters of 1.2 U_{eq}(N) or U_{eq}(C), respectively. The absolute structure could not be determined by crystallographic means due to the low scattering power of the light elements, so the Flack parameter, although close to zero, showed a high e.s.d. and, therefore, was meaningless. The results of the structure determinations are listed in Table 1 and Supporting Information, Table S1. The supplementary crystallographic data for this paper have been deposited with the Cambridge Structural database and are available free of charge via www.ccdc.cam.ac.uk/datarequest/cif on quoting the depository numbers CCCD-2024475 (100 K), CCDC-2024476 (200 K), and CCDC-2024477 (300 K). The crystal structure does undergo only slight changes between room temperature and 100 K. The most precise results obtained from the measurement at 100 K are discussed in the main part of this work; the results of the structure determinations at 200 K and at 300 K are presented in the Supporting Information (Tables S1–S8, Figure S1).

Table 1. Crystallographic data and details of the structure determination of γ-NADA at 100 K.

Compound	$C_6H_{12}N_2O_3$
crystal system	orthorhombic
space group	$P2_12_12_1$ (No. 19)
temperature	100(2) K
a	5.36470(10) Å
b	8.3652(2) Å
c	16.9149(5) Å
cell volume	759.09(3) Å^3
formula units	4
molar mass	160.18 g mol^{-1}
X-ray density	1.402 g·cm^{-3}
wavelength	Mo-Kα
absorption coefficient	0.112 mm^{-1}
measured reflections	39,700
unique reflections	5250
R_{int}	0.0273
2θ region	5.43°–84.10°
hkl range	$-10 \leq h \leq 10$
	$-11 \leq k \leq 15$
	$-31 \leq l \leq 31$
absorption correction	empirical
reflections > 2σ	4776
number of parameters	136
$R(F)$(obs), $R(F)$(all)	0.0293, 0.0348
$R_w(F^2)$(obs), $R_w(F^2)$(all)	0.0711, 0.0733
goodness of fit	1.025
max./min. difference density	0.408/−0.230 e·Å^{-3}
depository no.	CCDC 2024475

NMR spectra were measured with a Bruker Avance Ultrashield 400 MHz spectrometer. The ^{1}H spectra were calibrated by using the residual proton signal of the used deuterated solvents. Chemical shifts are reported in parts per million (ppm), with the solvent peaks serving as internal reference.

NMR Spectra (see Supporting Information Figures S2 and S3) of γ-NADA: ^{1}H-NMR (400 MHz, D_2O, 300 K): δ(ppm) = 3.71 (t, 1 H, CH), 3.36/3.30 (m, 2 H, CH_2), 2.10 (m, 2 H, CH_2), 1.99 (s, 3 H, CH_3); ^{13}C-NMR (101 MHz, D_2O, 300 K): δ(ppm) = 174.65 (COO), 174.15 (CON), 52.37 (CH), 35.38 (CH_2), 30.12 (CH_2), 21.74 ppm (CH_3).

Raman spectroscopy was performed in three independent measurements at room temperature with a Raman Senterra spectrometer from Bruker Optics, Germany. Solid crystals from cooling crystallization in H_2O, were placed on a microscope slide and measured with a 488 nm laser and 40 mW laser power.

The Fourier-transform infrared spectra (FTIR) were measured in three independent measurements at room temperature, using a Bruker ALPHA II FTIR spectrometer with the matching platinum attenuated total reflection (ATR) module. Crystals from cooling crystallization in H_2O were analyzed. Measurements were performed with 24 scans per sample and the baseline was subtracted via the rubber band method in the software OPUS. Raman bands and IR spectra were normalized to the most pronounced peak of 400 to 1700 cm^{-1} and 1701 to 4000 cm^{-1} for each measurement. More detailed assignments of the Raman and IR bands are presented in the Supporting Information section (Table S9).

3. Results

3.1. Crystal Shape and Structure

We crystallized γ-NADA in H_2O with cooling crystallization. Crystallinity of active substances in their final formulation is generally favorable for better physical and chemical stability, separation and process performance [40]. Figure 2 shows the obtained rod-shaped crystals of γ-NADA, crystallized in mL-reaction tubes (a) and in stirred 15 mL reactors (b). The shape of the crystal is the same—rod to needle-shaped—however, differing in size and arrangement. While crystals from the crystallization in reaction tubes with orbital shaking occur in clusters (Figure 2a), crystals from the reactor experiments with stirring are singled (Figure 2b).


(**a**)   (**b**)
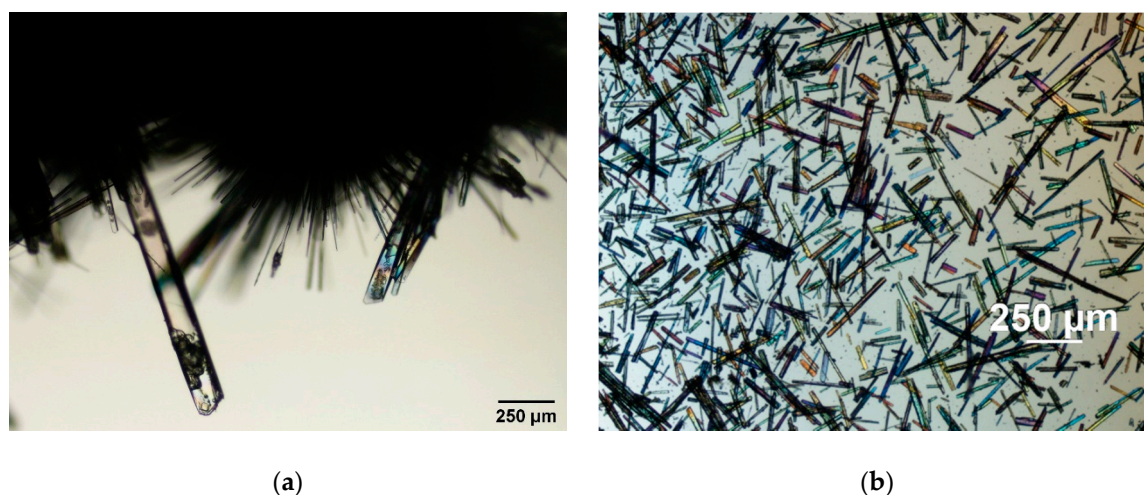
Figure 2. γ-NADA crystals obtained with cooling crystallization (50 °C–20 °C) in H_2O. (**a**) γ-NADA crystal cluster after crystallization in 2 mL reaction tube in H_2O with 300 rpm shaking. (**b**) Single crystals after crystallization in a small scale reactor with 150 rpm stirring and 10 mL volume.

Regarding bioavailability of active substances, the singled crystals from the 15 mL reactor system (b) are advantageous. They provide a better accessible surface compared to the clustered form. The increased surface-mass ratio with decreasing particle size improved the bioavailability;

however, the oxidation hazard can increase [41]. Further, downstream process steps can be affected by the appearance of the crystal [42], like the size, due to viscosity and rheology behavior. Especially needles and flakes are known to be difficult in process handling. Filtration, drying and formulation emerge more challenging. Thus, significant effort is made with, for example, wet-milling and temperature cycles to obtain bigger particle sizes but low aspect ratios and gain better process-ability of the needle-shaped crystals [43,44]. However, obtained crystals were composed only of γ-NADA, demonstrating that cooling crystallization is a versatile tool for the purification of this compatible solute in stirred reactors.

For the structure determination, a fragment of an approximately 3-mm-long needle has been isolated. Indexing of the diffraction pattern resulted in an orthorhombic unit cell, and inspection of symmetry and extinction conditions indicated unambiguously a non-centrosymmetry and the chiral space group $P2_12_12_1$, respectively. The results of the structure determination are given in Table 1 for the measurement at 100 K, and in the Supporting Information; Table S1 for 200 and 300 K. A symmetry cross-check with Platon [45] at the final state of the refinement confirmed this finding. Nγ-acetyl-L-2,4-diaminobutyric acid crystallizes with one formula as asymmetric unit. As almost usual for many amino acids [46], e.g., including the related ectoine and aspartic acid [47,48], the molecule, shown in Figure 3, is found in its zwitterionic form, so both oxygen atoms of the carboxylic acid group are deprotonated while the amine nitrogen atom at the α-C atom bears three H atoms (for detailed bond lengths and angles see Tables 2 and 3). The heavier atoms of the acetyl group, C6, C5, O3, and N2, are in-plane, indicating a partially delocalized π system. The methylene carbon atoms C3 and C4 are only slightly apart of this plane, too, e.g., shown by the bond angle sum of 359.13° around N2 and the C3–C4–N2–C5 torsion angle of 172.85°. The sp^3 carbon atoms C2, C3 and C4 are in almost perfect tetrahedral coordination (see Table 3) and are in skew conformation.
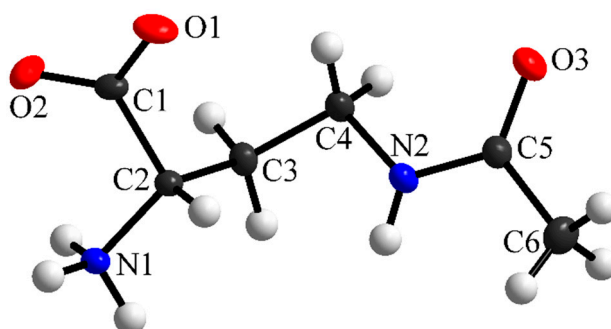
Figure 3. The γ-NADA molecule, obtained from a structure determination at 100 K. Atoms are drawn with anisotropic displacement ellipsoids of the non-hydrogen atoms as well as isotropic ones of the hydrogen atoms at the 80% probability level.

Table 2. Bond lengths for γ-NADA at 100 K, distances in Å.

Atoms	Distance	Atoms	Distance
C1–O1	1.2637(8)	C3–C4	1.5251(8)
C1–O2	1.2551(8)	C4–H4A	0.979(14)
C1–C2	1.5352(8)	C4–H4B	0.979(14)
C2–H2A	0.960(13)	C4–N2	1.4588(8)
C2–N1	1.4906(7)	N2–H2B	0.846(14)
N1–H1A	0.882(14)	N2–C5	1.3390(8)
N1–H1B	0.905(14)	C5–O3	1.2470(8)
N1–H1C	0.918(13)	C5–C6	1.5070(9)
C2–C3	1.5391(8)	C6–H6A	0.929(16)
C3–H3A	0.949(14)	C6–H6B	0.939(15)
C3–H3B	1.000(14)	C6–H6C	0.953(16)

Table 3. Bond angles for γ-NADA at 100 K, angles in °.

Atoms	Angle	Atoms	Angle
O2–C1–O1	126.72(6)	H3A–C3–H3B	108.2(12)
O2–C1–C2	116.49(5)	N2–C4–C3	110.08(5)
O1–C1–C2	116.75(6)	N2–C4–H4A	108.5(8)
N1–C2–C1	109.79(5)	C3–C4–H4A	113.7(8)
N1–C2–C3	108.09(5)	N2–C4–H4B	108.9(8)
C1–C2–C3	110.26(5)	C3–C4–H4B	109.5(8)
N1–C2–H2A	108.1(8)	H4A–C4–H4B	106.1(12)
C1–C2–H2A	110.5(9)	C5–N2–C4	120.80(5)
C3–C2–H2A	110.1(8)	C5–N2–H2B	119.3(10)
C2–N1–H1A	110.7(8)	C4–N2–H2B	119.1(10)
C2–N1–H1B	108.7(8)	O3–C5–N2	121.31(6)
H1A–N1–H1B	106.6(12)	O3–C5–C6	122.31(6)
C2–N1–H1C	111.4(8)	N2–C5–C6	116.35(5)
H1A–N1–H1C	111.0(12)	C5–C6–H6A	109.9(10)
H1B–N1–H1C	108.3(12)	C5–C6–H6B	112.3(9)
C4–C3–C2	113.38(5)	H6A–C6–H6B	106.3(14)
C4–C3–H3A	109.9(8)	C5–C6–H6C	109.5(11)
C2–C3–H3A	108.2(8)	H6A–C6–H6C	110.1(14)
C4–C3–H3B	109.1(8)	H6B–C6–H6C	108.7(12)
C2–C3–H3B	107.9(8)		

The γ-NADA molecules are packed in a more or less stretched manner with the main molecule extent parallel to the longest crystallographic axis *c*. They are connected via short and almost linear hydrogen bonds between the amino groups and oxygen atoms of neighboring molecules (see Table 4). All hydrogen atoms of the amino groups are part of one of these strong bonds, and the $NH_3^+\cdots O$ bonds are slightly shorter than the N2-H2B$\cdots$O3 bond. Considering these H bonds the NADA molecules form corrugated layers parallel to the *ac* plane shown in Figure 4a, which are interlinked three-dimensionally via the N1-H1A$\cdots$O1 bond (Figure 4b). The methyl group, as well as the two methylene groups C3 and C4, are oriented in the direction of the voids between the H bonds, forming sections of less polar character.

(a)　　　　　　　　　　　　　　　　　　　　(b)
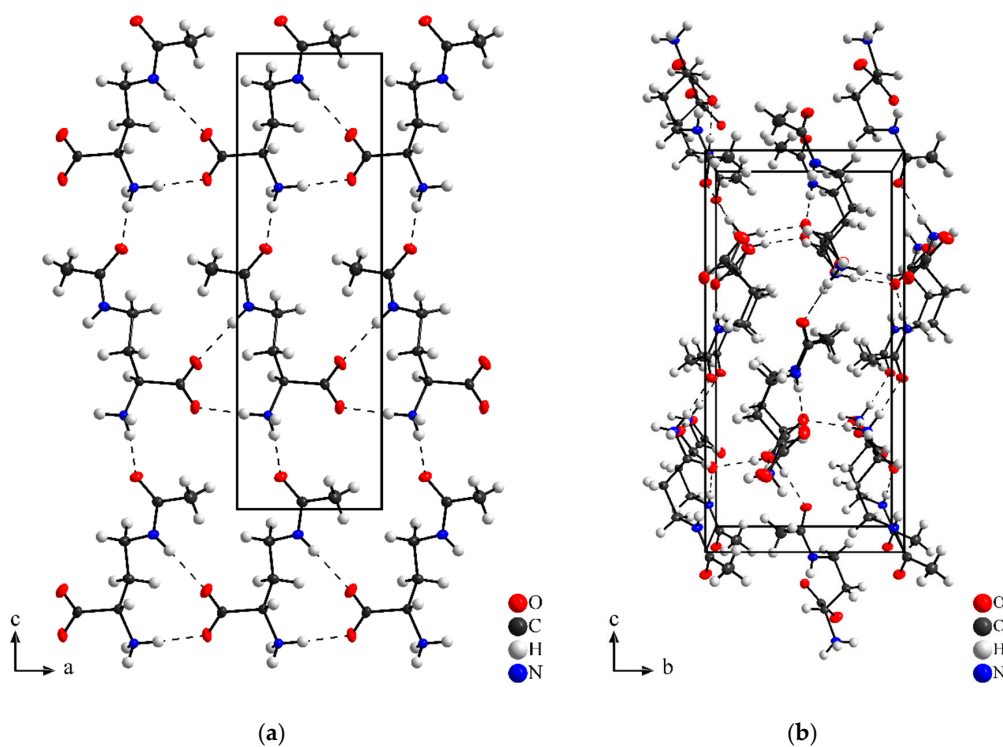
Figure 4. Crystal structure of γ-NADA at 100 K, view along [010] (**a**) and [–100] (**b**). Atoms are shown at the 80% probability level with carbon as black, hydrogen is white, oxygen as red, and nitrogen as blue ellipsoids. Strong H bonds are drawn as dashed lines.

**Table 4.** Hydrogen bond geometry for γ-NADA at 100 K, distances in Å, angles in °.

Atoms	*D*-H	H···*A*	*D*···*A*	*D*-H···*A*
N1–H1*A*···O1 [i]	0.882(14)	1.968(14)	2.8323(8)	166.2(13)
N1–H1*B*···O2 [ii]	0.905(14)	1.836(14)	2.7389(7)	176.4(12)
N1–H1*C*···O3 [iii]	0.918(13)	1.879(13)	2.7898(7)	171.8(13)
N2–H2*B*···O1 [ii]	0.846(14)	2.042(14)	2.8876(7)	176.7(14)

Symmetry codes: [i] −x + 1, y−1/2, −z + 1/2; [ii] x−1, y, z; [iii] −x + 1/2, −y + 1, z−1/2.

3.2. Raman and IR Spectra

Just as no crystal structure of Nγ-acetyl-L-2,4-diaminobutyric acid is available, there is a lack of further chemical characterization of this compatible solute. Thus, we performed Raman and IR measurements of the crystalline molecule, obtained from cooling crystallization in H_2O, to close this knowledge gap. Even though, Schütte and Schütz (1962) [49] assigned two IR bands for γ-NADA in nujol, namely the amide and NH vibration at 1650 cm^{-1} and 3280 cm^{-1}, respectively; the crystalline molecule has not been investigated yet.

Figure 5 shows both, normalized Raman (Figure 5a) and IR spectra (Figure 5b) of crystalline Nγ-acetyl-L-2,4-aminobutyric acid, gained from cooling crystallization in H_2O. The most intense Raman peaks show up at 2929 cm^{-1} in the wavenumber range of 1701–4000 cm^{-1} and at 1296 cm^{-1} and 910 cm^{-1} in the "fingerprint region" (400–1700 cm^{-1}) [50] of the amino acid derivative. Whereas the Raman spectra mostly shows single bands, the IR signal occurs in more clustered peaks. Here, the highest signal at 1537 cm^{-1} is part of an intense multi-peak area at 1200–1700 cm^{-1}. Further single peaks at 466 cm^{-1} and 3250 cm^{-1} and a second peak cluster with the maximum at 2959 cm^{-1} stand out. The characteristic groups of amino acids are, in general, the carboxyl (COOH/COO⁻) and the amino (NH_2/NH_3^+) group. Further, the carbonaceous residue side chain of γ-NADA includes a secondary amide group (O=C–NH–C) (see Figure 3). Thus, the Raman band at 2929 cm^{-1} with the two little shoulders at 2949 cm^{-1} and 2898 cm^{-1} and the IR peak cluster with the maximum at 2959 cm^{-1} (2800–3000 cm^{-1}) can be assigned to asymmetric and symmetric stretching of C-H (ν(CH)) [50–53] in CH, CH_2 and CH_3 groups of γ-NADA (Figure 3). However, in this region, overlapping with weak vibrations of NH_3^+ stretching $\nu(NH_3^+)$ is possible [50]. The intense Raman band at 1296 cm^{-1}, IR at 1300 cm^{-1}, are characteristic for the CH deformation modes δ(CH) [54]. Further bands at 3257 and 3250 cm^{-1} in Raman and IR, respectively might also represent slightly shifted N-H stretching (ν(NH)) in O=C–NH–C secondary amide [55]. Here, the Raman double peak between 1600–1700 cm^{-1} and the IR peak at 1628 cm^{-1} can be assigned to the stretching of the amide I carbonyl group ν(C=O). Bands of both, amide II stretching of C–N ν(C–N) and planar bending of N-H (δ(N-H)) are found in a wavenumber range of 1480 to 1580 cm^{-1} [52,56]. Thus, the outstanding peak at the IR fingerprint region at 1537 cm^{-1}, which is also visible in Raman spectroscopy (1538 cm^{-1}), can be identified as symmetric bending of the amino group $\delta(NH_3^+)$ [57]. The asymmetric bending ($\delta_{as}(NH_3^+)$) can be assigned to the Raman and IR bands at 1588 cm^{-1}, yet also overlapping with the stretching of the characteristic carboxyl group $\nu_{as}(COO^-)$. The symmetric stretching $\nu_s(COO^-)$ occurs at 1419 cm^{-1} and 1411 cm^{-1} for Raman and IR, respectively. In the lower wavenumber range OH and NH wag can be assigned to bands at 900–770 cm^{-1} for primary amines, 750–680 cm^{-1} for secondary amines and 750–550 cm^{-1} for amides. Further, the detailed assignment is summarized in the Supporting Information Table S9.
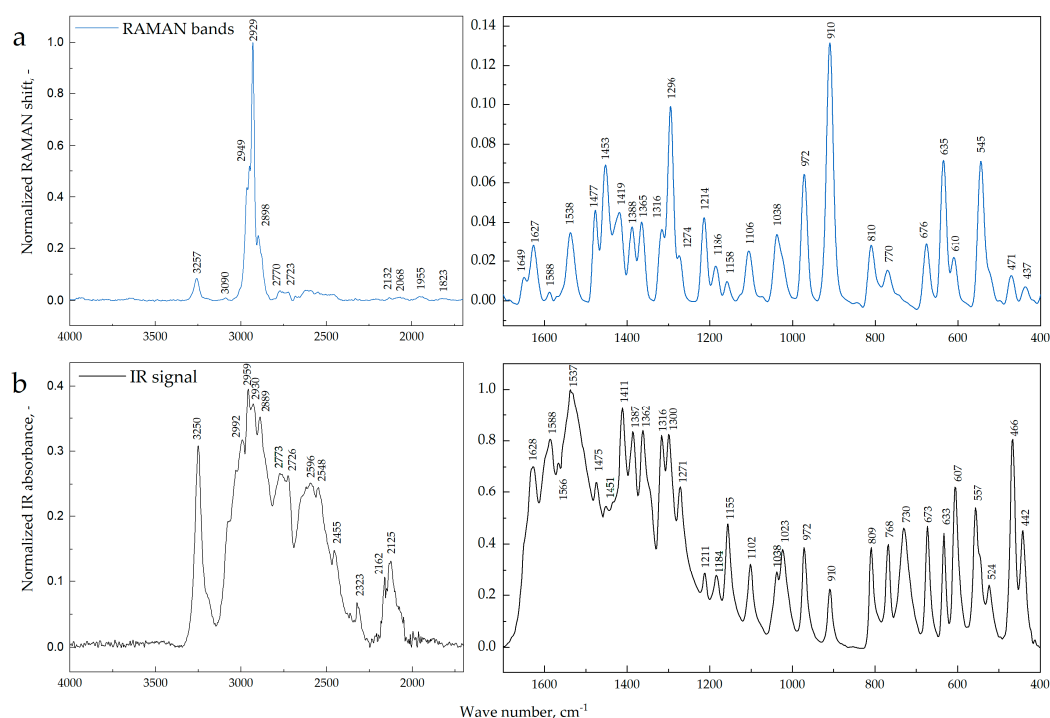
Figure 5. Raman (**a**) and IR spectra (**b**) of crystalline Nγ-acetyl-L-2,4-diaminobutyric acid, obtained from cooling crystallization in H_2O. The signal was normalized to the most pronounced peak, namely at 2929 cm^{-1} and 1537 cm^{-1} for Raman and IR spectroscopy, respectively. For the detailed assignment of the bands, see Table S9.

4. Conclusions

We showed that Nγ-acetyl-L-2,4-diaminobutyric acid (γ-NADA) could successfully be crystallized in H_2O with cooling crystallization, generating rod-shaped crystals. Variations in volume and stirring conditions lead to differently sized and arranged crystals, namely in clusters or singles. With crystal structure determination, the molecule was found to be zwitterionic and partly polar, both characteristic attributes of compatible solutes. Further, the compound crystallizes in the chiral orthorhombic space group $P2_12_12_1$ with all atoms at general positions and forms an extended three-dimensional network of hydrogen bonds. Besides, XRD structure determination proofed the crystals to be free from intra-crystalline impurities, sparing elaborated recrystallization in a possible future separation process. The measured spectral bands of Raman, IR, ^{1}H NMR and ^{13}C NMR can be assigned to all required chemical groups of γ-NADA, thus verifying the crystals to be the aimed compatible solutes without included impurities. To our knowledge neither the structure nor full spectroscopic analysis with Raman and IR have been published yet, thus we make it usable as reference material. Also ^{1}H NMR and ^{13}C NMR spectra of the pure compound are not available yet, however Cánovas et al. [34,36] showed a ^{13}C NMR spectrum of the cell extract of a γ-NADA producing mutant strain. Here, the assigned γ-NADA bands are in good agreement with our spectrum.

With this a first step was done to move γ-NADA more in the focus of interest when developing new active substances based on compatible solutes. With regard to a biotechnological process for γ-NADA, the results of shape, size and structure can be used for appropriate adjustments. Our results show an easy crystallization in H_2O and with this, a good purification of γ-NADA without any included impurities in the crystalline substance; however, rod and needle-shaped crystals are known to be more difficult in process handling. Here, with adaptive strategies like wet-milling and adjusted temperature cycles, disadvantages can be overcome [43,44].

selected bond lengths and angles at 200 K/300 K; Raman and IR band assignments for γ-NADA crystals, measured at room temperature, obtained from cooling crystallization in water; ^{1}H NMR and ^{13}C NMR spectra.

References

1. Brown, A.D. Microbial water stress. *Bacteriol. Rev.* **1976**, *40*, 803–846. [CrossRef] [PubMed]
2. Crowley, E. Compatible solute ectoine review: Protection mechanisms and production methods. *J. Undergrad. Stud. Trent* **2017**, *5*, 32–39.
3. Sahle, C.J.; Schroer, M.A.; Jeffries, C.M.; Niskanen, J.; Salmannejad, F.; Nafissi-Varcheh, N.; Tran, B.H.; Dao, V.A.; Bilstein, A.; Unfried, K.; et al. Hydration in aqueous solutions of ectoine and hydroxyectoine. *Phys. Chem. Chem. Phys.* **2018**, *20*, 27917–27923. [CrossRef] [PubMed]
4. Smiatek, J.; Harishchandra, R.K.; Rubner, O.; Galla, H.-J.; Heuer, A. Properties of compatible solutes in aqueous solution. *Biophys. Chem.* **2012**, *160*, 62–68. [CrossRef]
5. Panuszko, A.; Bruździak, P.; Kaczkowska, E.; Stangret, J.; Rieckmann, T.; Gatzemeier, F.; Christiansen, S.; Rothkamm, K.; Münscher, A. General mechanism of osmolytes' influence on protein stability irrespective of the type of osmolyte cosolvent. *J. Phys. Chem. B* **2016**, *120*, 11159–11169. [CrossRef]
6. Zeman, J.; Holm, C.; Smiatek, J. The effect of small organic cosolutes on water structure and dynamics. *J. Chem. Eng. Data* **2019**, *65*, 1197–1210. [CrossRef]
7. Galinski, E.A. Compatible solutes of halophilic eubacteria: Molecular principles, water-solute interaction, stress protection. *Experientia* **1993**, *49*, 487–496. [CrossRef]
8. Galinski, E.A.; Gunde-Cimerman, N.; Plemenitaš, A.; Oren, A.; Kets, E.; Teunissen, P.; de Bont, J. Osmoadaptation in bacteria. *Adv. Microb. Physiol.* **1995**, *37*, 272–328. [CrossRef]
9. Roberts, M.F. Organic compatible solutes of halotolerant and halophilic microorganisms. *Saline Syst.* **2005**, *1*, 5. [CrossRef]
10. Kunte, H.J. Osmoregulation in bacteria: Compatible solute accumulation and osmosensing. *Environ. Chem.* **2006**, *3*, 94–99. [CrossRef]
11. Gunde-Cimerman, N.; Plemenitaš, A.; Oren, A.; Kets, E.; Teunissen, P.; de Bont, J. Strategies of adaptation of microorganisms of the three domains of life to high salt concentrations. *FEMS Microbiol. Rev.* **2018**, *42*, 353–375. [CrossRef] [PubMed]
12. da Costa, M.S.; Santos, H.; Galinski, E.A. An overview of the role and diversity of compatible solutes in Bacteria and Archaea. In *Biotechnology of Extremophiles*; Springer: Berlin/Heidelberg, Germany, 1998; pp. 117–153.
13. Lippert, K.; Galinski, E.A. Enzyme stabilization be ectoine-type compatible solutes: Protection against heating, freezing and drying. *Appl. Microbiol. Biotechnol.* **1992**, *37*, 61–65. [CrossRef]
14. Borges, N.; Ramos, A.; Raven, N.D.; Sharp, R.J.; Santos, H.; Brown, A.D. Comparative study of the thermostabilizing properties of mannosylglycerate and other compatible solutes on model enzymes. *Extremophiles* **2002**, *6*, 209–216. [CrossRef]
15. Marini, A.; Reinelt, K.; Krutmann, J.; Bilstein, A.; Panuszko, A.; Bruździak, P.; Kaczkowska, E.; Stangret, J.; Rieckmann, T.; Gatzemeier, F.; et al. Ectoine-containing cream in the treatment of mild to moderate atopic dermatitis: A randomised, comparator-controlled, intra-individual double-blind, multi-center trial. *Ski. Pharm. Physiol.* **2014**, *27*, 57–65. [CrossRef] [PubMed]
16. Heider, L.; Hamasaki, T.; Masaki, H. Use of Compatible Solutes. U.S. Patent 2020/0030214 A1, 30 January 2020.

17. Tran, B.H.; Dao, V.A.; Bilstein, A.; Unfried, K.; Shah-Hosseini, K.; Mösges, R. Ectoine-containing inhalation solution versus saline inhalation solution in the treatment of acute bronchitis and acute respiratory infections: A prospective, controlled, observational study. *BioMed Res. Int.* **2019**, *2019*, 7945091. [CrossRef] [PubMed]

18. Unfried, K.; Krämer, U.; Sydlik, U.; Autengruber, A.; Bilstein, A.; Stolz, S.; Marini, A.; Schikowski, T.; Keymel, S.; Krutmann, J. Reduction of neutrophilic lung inflammation by inhalation of the compatible solute ectoine: A randomized trial with elderly individuals. *Int. J. Chron. Obs. Pulmon. Dis.* **2016**, *11*, 2573–2583. [CrossRef] [PubMed]

19. Rieckmann, T.; Gatzemeier, F.; Christiansen, S.; Rothkamm, K.; Münscher, A. The inflammation-reducing compatible solute ectoine does not impair the cytotoxic effect of ionizing radiation on head and neck cancer cells. *Sci. Rep.* **2019**, *9*, 6594. [CrossRef] [PubMed]

20. Dao, V.A.; Bilstein, A.; Overhagen, S.; Géczi, L.; Baráth, Z.; Mösges, R. Effectiveness, tolerability, and safety of ectoine-containing mouthwash versus those of a calcium phosphate mouthwash for the treatment of chemotherapy-induced oral mucositis: A prospective, active-controlled, non-interventional study. *Oncol. Ther.* **2018**, *6*, 59–72. [CrossRef]

21. Barth, S.; Huhn, M.; Matthey, B.; Klimka, A.; Galinski, E.A.; Engert, A. Compatible-solute-supported periplasmic expression of functional recombinant proteins under stress conditions. *Appl. Environ. Microbiol.* **2000**, *66*, 1572–1579. [CrossRef]

22. Salmannejad, F.; Nafissi-Varcheh, N.; Tran, B.H.; Dao, V.A.; Bilstein, A.; Unfried, K.; Shah-Hosseini, K.; Mösges, R. Ectoine and hydroxyectoine inhibit thermal-induced aggregation and increase thermostability of recombinant human interferon Alfa2b. *Eur. J. Pharm. Sci.* **2017**, *97*, 200–207. [CrossRef]

23. Barth, S. Pharmaceutical Formulation. U.S. Patent 7,147,849 B2, 12 December 2006.

24. Kets, E.; Teunissen, P.; de Bont, J. Effect of compatible solutes on survival of lactic Acid bacteria subjected to drying. *Appl. Environ. Microbiol.* **1996**, *62*, 259–261. [CrossRef] [PubMed]

25. Weinbuch, D.; Hawe, A.; Jiskoot, W.; Friess, W. Introduction into formulation development of biologics. In *Challenges in Protein Product Development*; Springer: Berlin/Heidelberg, Germany, 2018; pp. 3–22.

26. Wang, W.; Ohtake, S. Science and art of protein formulation development. *Int. J. Pharm.* **2019**, *568*, 118505. [CrossRef] [PubMed]

27. Barnett, G.V.; Razinkov, V.I.; Kerwin, B.A.; Blake, S.; Qi, W.; Curtis, R.A.; Roberts, C.J. Osmolyte effects on monoclonal antibody stability and concentration-dependent protein interactions with water and common osmolytes. *J. Phys. Chem. B* **2016**, *120*, 3318–3330. [CrossRef] [PubMed]

28. Miyawaki, O.; Dozen, M.; Nomura, K. Thermodynamic analysis of osmolyte effect on thermal stability of ribonuclease A in terms of water activity. *Biophys. Chem.* **2014**, *185*, 19–24. [CrossRef]

29. Kunte, H.J.; Lentzen, G.; Galinski, E. Industrial production of the cell protectant ectoine: Protection mechanisms, processes, and products. *Curr. Biotechnol.* **2014**, *3*, 10–25. [CrossRef]

30. Vreeland, R.H.; Litchfield, C.; Martin, E.; Elliot, E. Halomonas elongata, a new genus and species of extremely salt-tolerant bacteria. *Int. J. Syst. Evol. Microbiol.* **1980**, *30*, 485–495. [CrossRef]

31. Ono, H.; Sawada, K.; Khunajakr, N.; Tao, T.; Yamamoto, M.; Hiramoto, M.; Shinmyo, A.; Takano, M.; Murooka, Y. Characterization of biosynthetic enzymes for ectoine as a compatible solute in a moderately halophilic eubacterium, Halomonas elongata. *J. Bacteriol.* **1999**, *181*, 91–99. [CrossRef]

32. Schwibbert, K.; Marin-Sanguino, A.; Bagyan, I.; Heidrich, G.; Lentzen, G.; Seitz, H.; Rampp, M.; Schuster, S.C.; Klenk, H.P.; Pfeiffer, F.; et al. A blueprint of ectoine metabolism from the genome of the industrial producer Halomonas elongata DSM 2581 T. *Environ. Microbiol.* **2011**, *13*, 1973–1994. [CrossRef]

33. Liss, I. N-Acetyldiaminobuttersäure, eine neue Aminosäure aus dem Latex von Euphorbia pulcherrima Willd ex Klotzsch. *Phytochemistry* **1962**, *1*, 87–88. [CrossRef]

34. Cánovas, D.; Vargas, C.; Iglesias-Guerra, F.; Csonka, L.N.; Rhodes, D.; Ventosa, A.; Nieto, J.J.; Cánovas, D.; Borges, N.; Vargas, C.; et al. Isolation and characterization of salt-sensitive mutants of the moderate halophile Halomonas elongata and cloning of the ectoine synthesis genes. *J. Biol. Chem.* **1997**, *272*, 25794–25801. [CrossRef]

35. García-Estepa, R.; Cánovas, D.; Iglesias-Guerra, F.; Ventosa, A.; Csonka, L.N.; Nieto, J.J.; Vargas, C. Osmoprotection of Salmonella enterica serovar Typhimurium by Ngamma-acetyldiaminobutyrate, the precursor of the compatible solute ectoine. *Syst. Appl. Microbiol.* **2006**, *29*, 626–633. [CrossRef] [PubMed]

36. Cánovas, D.; Borges, N.; Vargas, C.; Ventosa, A.; Nieto, J.J.; Santos, H. Role of Ngamma-acetyldiaminobutyrate as an enzyme stabilizer and an intermediate in the biosynthesis of hydroxyectoine. *Appl. Environ. Microbiol.* **1999**, *65*, 3774–3779. [CrossRef] [PubMed]

37. Myerson, A.S. *Handbook of Industrial Crystallization*; Butterworth-Heinemann: Boston, MA, USA, 2002.

38. Sheldrick, G.M. A short history of SHELX. *Acta Cryst. A* **2008**, *64*, 112–122. [CrossRef] [PubMed]
39. Sheldrick, G.M. Crystal structure refinement with SHELXL. *Acta Cryst. C Struct. Chem.* **2015**, *71*, 3–8. [CrossRef]
40. Variankaval, N.; Cote, A.S.; Doherty, M.F. From form to function: Crystallization of active pharmaceutical ingredients. *AICHE J.* **2008**, *54*, 1682–1688. [CrossRef]
41. Kirwan, D.J.; Orella, C.J. Crystallization in the pharmaceutical and bioprocessing industries. In *Handbook of Industrial Crystallization*, 2nd ed.; Myerson, A.S., Ed.; Butterworth-Heinemann: Boston, MA, USA, 2002; pp. 249–266.
42. Wibowo, C.; Chang, W.C.; Ng, K.M. Design of integrated crystallization systems. *AICHE J.* **2001**, *47*, 2474–2492. [CrossRef]
43. Perini, G.; Salvatori, F.; Ochsenbein, D.R.; Mazzotti, M.; Vetter, T. Filterability prediction of needle-like crystals based on particle size and shape distribution data. *Sep. Purif. Technol.* **2019**, *211*, 768–781. [CrossRef]
44. Wilson, D.; Bunker, M.; Milne, D.; Jawor-Baczynska, A.; Powell, A.; Blyth, J.; Streather, D. Particle engineering of needle shaped crystals by wet milling and temperature cycling: Optimisation for roller compaction. *Powder Technol.* **2018**, *339*, 641–650. [CrossRef]
45. Spek, A.L. Structure validation in chemical crystallography. *Acta Cryst. D Biol. Cryst.* **2009**, *65*, 148–155. [CrossRef]
46. Görbitz, C.H. Crystal structures of amino acids: From bond lengths in glycine to metal complexes and high-pressure polymorphs. *Crystallogr. Rev.* **2015**, *21*, 160–212. [CrossRef]
47. Schuh, W.; Puff, H.; Galinski, E.A.; Trüper, H.G. Die Kristallstruktur des Ectoin, einer neuen osmoregulatorisch wirksamen Aminosäure/the crystal structure of ectoine, a novel amino acid of potential osmoregulatory function. *Z. Für Nat. C* **1985**, *40*, 780–784. [CrossRef]
48. Derissen, J.L.; Endeman, H.J.; Peerdeman, A.F. The crystal and molecular structure of L-aspartic acid. *Acta Crystallogr. Sect. B Struct. Crystallogr. Cryst. Chem.* **1968**, *24*, 1349–1354. [CrossRef]
49. Schütte, H.R.; Schütz, W. Synthese von Nγ-Acetyl-ornithin und Nδ-Acetyl-Diaminobuttersäure. *Justus Liebigs Ann. Chem.* **1963**, *665*, 203–204. [CrossRef]
50. Jenkins, A.L.; Larsen, R.A.; Williams, T.B.; Howell, N.K.; Arteaga, G.; Nakai, S.; Li-Chan, E.C. Characterization of amino acids using Raman spectroscopy. *Spectrochim. Acta A Mol. Biomol. Spectrosc.* **2005**, *61*, 1585–1594. [CrossRef] [PubMed]
51. Larkin, P.J. General outline for IR and raman spectral interpretation. In *Infrared and Raman Spectroscopy*, 2nd ed.; Larkin, P.J., Ed.; Elsevier: Amsterdam, The Netherlands, 2018; pp. 135–151.
52. Morhardt, C.; Ketterer, B.; Heißler, S.; Franzreb, M. Direct quantification of immobilized enzymes by means of FTIR ATR spectroscopy—A process analytics tool for biotransformations applying non-porous magnetic enzyme carriers. *J. Mol. Catal. B Enzym.* **2014**, *107*, 55–63. [CrossRef]
53. Howell, N.K.; Arteaga, G.; Nakai, S.; Li-Chan, E.C. Raman spectral analysis in the C-H stretching region of proteins and amino acids for investigation of hydrophobic interactions. *J. Agric. Food Chem.* **1999**, *47*, 924–933. [CrossRef] [PubMed]
54. Schwaminger, S.P.; Fraga García, P.; Merck, G.K.; Bodensteiner, F.A.; Heissler, S.; Günther, S.; Berensmeier, S. Nature of interactions of amino acids with bare magnetite nanoparticles. *J. Phys. Chem. C* **2015**, *119*, 23032–23041. [CrossRef]
55. Larkin, P.J. IR and Raman spectra-structure correlations: Characteristic group frequencies. In *Infrared and Raman Spectroscopy*, 2nd ed.; Larkin, P.J., Ed.; Elsevier: Amsterdam, The Netherlands, 2018; pp. 85–134.
56. Mallamace, F.; Corsaro, C.; Mallamace, D.; Vasi, S.; Vasi, C.; Dugo, G. The role of water in protein's behavior: The two dynamical crossovers studied by NMR and FTIR techniques. *Comput. Struct. Biotechnol. J.* **2015**, *13*, 33–37. [CrossRef]
57. Lambert, J.B.; Shurvell, H.F.; Lightner, D.A.; Cooks, R.G. *Introduction to Organic Spectroscopy*; Macmillan: New York, NY, USA, 1987.